

See discussions, stats, and author profiles for this publication at: <https://www.researchgate.net/publication/239414671>

Tonal and Broadband Noise Calculations for Aeroacoustic Optimization of a Pusher Propeller

Article in *Journal of Aircraft* · May 2010

DOI: 10.2514/1.45315

CITATIONS

22

READS

660

4 authors, including:



Pagano Antonio

CIRA Centro Italiano Ricerche Aerospaziali

22 PUBLICATIONS 71 CITATIONS

[SEE PROFILE](#)



Mattia Barbarino

CIRA Centro Italiano Ricerche Aerospaziali

27 PUBLICATIONS 117 CITATIONS

[SEE PROFILE](#)



Damiano Casalino

Exa Corporation

103 PUBLICATIONS 1,378 CITATIONS

[SEE PROFILE](#)

Some of the authors of this publication are also working on these related projects:



Digital Aircraft Noise Certification [View project](#)



Trailing edge noise reduction [View project](#)

Tonal and Broadband Noise Calculations for Aeroacoustic Optimization of a Pusher Propeller

Antonio Pagano,* Mattia Barbarino,* Damiano Casalino,† and Luigi Federico*
Centro Italiano Ricerche Aerospaziali, 81043 Capua, Italy

DOI: 10.2514/1.45315

A multidisciplinary analysis and optimization is carried out for a propeller in a real pusher aircraft configuration with the goal of reducing the radiated noise power levels, while preserving the aerodynamic efficiency. The optimization process involves the shape of the blade and the position of the engine exhaust ducts. A coupling of the unsteady aerodynamic and structural-dynamic blade models provides the aeroelastic propeller model that drives a tonal and broadband aeroacoustic prediction. The tonal noise results from the periodic flow unsteadiness due to the nonaxial flight and to the impingement of the engine exhausts on the propeller disk. The broadband noise is mainly due to the interaction between the blade leading edge and the exhaust turbulence. It is shown that the tonal noise overwhelms the broadband noise and that the optimization affects the shape of the blade at the tip and in the spanwise segment hit by the exhausts. An overall sound pressure level reduction of 3.5 dB is achieved at the takeoff condition, while preserving the design propeller thrust and resulting in a small penalty on the propeller efficiency in cruise.

Nomenclature

a	=	speed of sound
B	=	number of blades
C_N	=	normal force coefficient, $(dN/dr)/(qc)$
C_T	=	thrust coefficient, $T/16\rho n^2 R^4$
C_p	=	pressure coefficient, $(p - p_s)/q$
c	=	blade local chord
k	=	acoustic wave number
L	=	blade local span
M	=	Mach number
$M_{\Omega R}$	=	rotational Mach number
N	=	sectional normal force
n	=	rotations per minute
p	=	flow pressure
p_s	=	flow static pressure
Q	=	rotor torque
q	=	dynamic pressure, $0.5\rho U^2$
R	=	blade radius
r	=	blade local radius
S_{pp}	=	noise power spectral density
T	=	rotor thrust
U	=	streamwise velocity
\mathbf{v}	=	flow velocity
\mathcal{R}	=	gas constant
\mathcal{T}	=	flow temperature
γ	=	ratio of heats
η	=	aerodynamic efficiency, $(TU)/(Q\Omega)$
θ_{75}	=	pitch angle at 75% of blade radius
μ	=	rotor advance ratio, $U/(\Omega R)$
ρ	=	flow density
ϕ	=	velocity potential
ϕ_{pp}	=	wall-pressure power spectral density
ϕ_{ww}	=	velocity power spectral density
Ω	=	rotor rotational speed, $(\pi n)/30$

ω = acoustic radian frequency

Subscripts

j	=	jet centerline quantities
t	=	partial time derivative
0	=	freestream quantities

Superscripts

/	=	perturbation quantities
.	=	time derivative
-	=	nondimensional quantities

I. Introduction

IN THE framework of the national research project ACADEMIA (Advanced Computational Aerodynamic Environment for Multidisciplinary Integrated Analysis), the Centro Italiano Ricerche Aerospaziali (CIRA) has developed a multidisciplinary analysis (MDA) and optimization methodology for helicopter rotors and propellers. This methodology was applied in the context of the European Commission (EC)-funded project CESAR (Cost-Effective Small Aircraft) to optimize the acoustic and aerodynamic performances of a pusher propeller provided by Piaggio Aero and derived from the propulsive system of the turboprop business aircraft P180 [1]. The present work illustrates the subsequent efforts undertaken by CIRA on the methodology improvements and on the extension of the propeller design space.

The P180 is well known in the aeronautical community for its efficiency with respect to small turbojets that operate in the same market sector. Thanks to the rear location of the propeller disks with respect to the passenger seats, the interior noise is lower than for any turbojet or turboprop business aircraft. However, due to the strongly perturbed flow in which the pusher propellers operate, the exterior noise of this configuration is the upper limit of the acceptable range. The influence of the wing wake and engine exhausts on the noise emitted by the pusher propellers has been investigated in the past both numerically [2] and experimentally [3]. Schematic views of the P180 wing–nacelle configuration are shown in Fig. 1.

Within the CESAR project the main focus was on the application of numerical technologies to design a new propeller able to reduce the noise levels by 3 dB (at least), while preserving good cruise performance characteristics. From preliminary studies it turned out that the original five-blade propeller could be changed in favor of a six-blade configuration rotating at a reduced angular velocity. That propeller was selected as baseline configuration for the optimization

Presented as Paper 3138 at the 15th AIAA/CEAS Aeroacoustics Conference, Miami, FL, 11–13 May 2009; received 6 May 2009; revision received 12 January 2010; accepted for publication 13 January 2010. Copyright © 2010 by the Centro Italiano Ricerche Aerospaziali (CIRA). Published by the American Institute of Aeronautics and Astronautics, Inc., with permission. Copies of this paper may be made for personal or internal use, on condition that the copier pay the \$10.00 per-copy fee to the Copyright Clearance Center, Inc., 222 Rosewood Drive, Danvers, MA 01923; include the code 0021-8669/10 and \$10.00 in correspondence with the CCC.

*Research Engineer, Rotorcraft. Member AIAA.

†Research Engineer, Aerodynamic and Aeroacoustic Methods. Member AIAA.

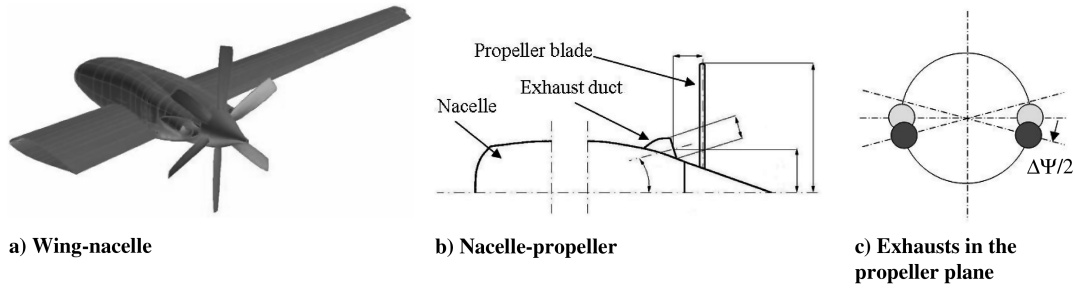


Fig. 1 P180 wing-engine system. On the right figure, the baseline and modified exhaust configurations are pictured in light and dark gray, respectively.

studies performed by CIRA that led to a modification of the blade planform in the tip region [1]. The analysis involved an aeroelastic and an aeroacoustic model of the blade that provides the propeller aerodynamic performances and radiated tonal noise to an automatic optimization software. A similar analysis is applied in the present work with the goal of extending the shape optimization to the spanwise segment of the blade hit by the engine exhaust. In addition, the broadband noise generated by the blades is estimated through a semi-analytical model that accounts for the self-noise from the trailing edge and the blade-turbulence interaction noise from the leading edge.

As discussed in [1], one of the preliminary outcomes of the optimization study was that the six-blade propeller is 2 dB quieter than the five-blade one and that this noise reduction is due to the lower tip speed. Indeed, the prediction of the noise generated by the same isolated propellers revealed that the engine exhausts cause an increase of 9 and 14 dB for the five- and six-blade propellers, respectively. This significantly different installation effect is due to the simultaneous blade-exhaust interactions occurring in the six-blade propeller. For this reason it has been decided in the present work to investigate the effects on the radiated noise due to an angular shift of the exhaust ducts, as sketched in Fig. 1c.

The geometric parameterization of a propeller blade results in a large design space. For this reason, a suitable aerodynamic model for automatic optimizations must be sufficiently fast, but able to properly describe the effects due to the rigid and elastic motion of the blade, the compressibility effects at the blade tip, and the aerodynamic losses occurring in the turbulent boundary layers. Hence, it has been decided to employ a rotorcraft full-potential computational fluid dynamics (CFD) model [4], strongly coupled with a turbulent boundary-layer model based on the defect-formulation theory developed by Le Balleur [5,6]. The boundary-layer model permits computing the propeller aerodynamic characteristics and provides the integral quantities required by a semi-analytical broadband noise model. The broadband noise levels are added to the tonal noise levels computed by applying a Ffowcs Williams and Hawkins (FW-H) acoustic analogy [7] to the wall-pressure distribution.

The layout of the paper is as follows. In Sec. II a general description of the baseline configuration and reference flight conditions is provided. The MDA process and optimization strategy is outlined in Sec. III. Then the aerodynamic, elastic, and aeroacoustic models are presented in Secs. IV, V, and VI, with emphasis on the broadband noise model that represents the original contribution of this work with respect to the previous one [1]. The results of the optimization study are discussed in Sec. VII, followed by some concluding remarks.

II. Pusher-Propeller Baseline Configuration

The baseline configuration has been released by Piaggio Aero after preliminary design studies undertaken in the CESAR project. As sketched in Fig. 1, a six-blade propeller is considered and its angular velocity is set to 188.5 rad/s, corresponding to a blade passage frequency of 180 Hz. This propeller has been obtained by using the same blade of a five-blade production propeller that rotates at a higher velocity. Therefore, a shape optimization is required to adapt the new propeller to the different operating conditions.

The optimization is carried out by considering two flight conditions: the takeoff condition, corresponding to a flight altitude of 914 m and Mach number $M = 0.235$, for which the propulsion system is required to produce a thrust of 6280 N, and the cruise condition, corresponding to a flight altitude of 7620 m and Mach number $M = 0.58$, for which the propulsion system is required to produce a thrust of 2800 N.

As sketched in Fig. 1c, the exhaust centerlines are diametrically opposite in the propeller plane. This is responsible for a higher jet-propeller interaction noise in the case of a six-blade propeller. It has been therefore decided to estimate the effects of a new exhaust configuration obtained by introducing an angular skew in the two trace disks of the jets in the propeller plane.

III. Optimization Process: Objectives and Constraints

This section is devoted to the description of the MDA process that provides the influence of the blade geometry on the aerodynamic performances and noise of the pusher propeller. The optimization strategy that drives the MDA process toward a set of blade configurations that meets the required targets while satisfying some geometrical and performance constraints is also described.

A. MDA Process

To compute the noise generated by a pusher propeller with an adequate confidence level, a suitable aeroelastic model of the blade must be matched with an aeroacoustic model. Because of the high flow unsteadiness, mainly caused by the exhaust impinging on the propeller disk and by the elastic-blade response, the aeroelastic model of the blade is provided by a weak coupling between a computational structural dynamics (CSD) code and a CFD code. The aeroacoustic model extrapolates the blade pressure distribution and boundary-layer turbulent quantities into far-field acoustic levels. The exhaust jets are modeled by using self-similar velocity profiles: that is,

$$U(\tilde{r}, \tilde{z}) = 0.5(U_j + U_0)[1 - (U_j - U_0)\text{erf}(13\tilde{r}/\tilde{z})/(U_j + U_0)]$$

where \tilde{r} is the radial distance from the jet centerline, \tilde{z} is the axial distance from the nozzle, U_j is the flow velocity on the jet centerline, and U_0 is the freestream velocity.

The CSD-CFD weak coupling consists of the following steps:

- 1) The CSD code for a given thrust coefficient C_T provides the first estimation of the pitch angle (θ_{75}), power coefficient C_P , and efficiency η .
- 2) For the computed value of θ_{75} , the CSD code also provides the blade elastic deformations and the induced velocities on the blade due to the wake structure.
- 3) The CFD code accepts in input θ_{75} , the blade elastic deformations, and the induced velocities (as an inflow model) and computes the sectional blade aerodynamic coefficients.
- 4) The CSD code uses the CFD aerodynamic coefficients (C_l , C_m , and C_d) to update the internal 2-D aerodynamics so that a new estimate of θ_{75} , C_P , and η is provided.
- 5) A convergence criterion on θ_{75} is checked, and if it is not satisfied, the process control is sent to step 2.

The aeroacoustic model is based on two distinct approaches: one for the tonal noise the other one for the broadband noise. The tonal noise is computed from the unsteady blade pressure distribution provided by the CFD code by means of a time-domain integral solution of the FW-H equation [7], put forward by Farassat and Succi [8]. Only the linear source terms due to the unsteady force exerted by the propeller on the surrounding fluid and mass flow displacement due to the blade motion are accounted for. The broadband noise is computed through semi-analytical models that permit converting statistical flow quantities in proximity of the blade trailing and leading edges into far-field noise spectral levels. The near- to far-field extrapolation model is derived from flat-plate unsteady aerodynamic theories and acoustic scattering formulas that have been proposed in [9–12] and successively improved in [13–15]. The near-field flow quantities required by these models are the wall-pressure spectrum and boundary-layer thickness and asymptotic flow velocity close to the trailing edge (self-noise) and the velocity spectrum and integral scale of the turbulence convected past the blade leading edge (turbulence interaction noise).

All the codes and tools involved in the outlined MDA process have been developed by CIRA in the framework of several research programs focused on rotorcraft aerodynamics, structural dynamics, and aeroacoustics. A brief description of the mathematical formulation implemented in each code is provided in Secs. IV, V, and VI.

B. Optimization Environment

The commercial optimization tool OPTIMUS [16], developed by Noesis Solutions, has been used for the present study. This software offers a powerful graphical environment that permits to integrate arbitrary analysis codes, automate the process execution, control the data exchange between multidisciplinary codes, split the process over a heterogeneous computational environment (in which analysis codes run on different computer platforms), and postprocess the analysis and optimization results. The key functionalities of several optimization methods are fully exploited to address the search of global and local optimal solutions. Design of experiment (DOE) and response surface model (RSM) techniques are available for the definition and exploration of the design space. The design optimization can be carried through genetic, gradient, and coupled genetic/gradient algorithms.

C. Blade Shape Parameterization

A key element of an efficient automated design optimization of a propeller is the definition of a suitable parametric model of the blade geometry [17]. The general goal is to reduce the number of design variables while retaining the ability to cover a global range of design solutions. The common approach consists of modeling the blade surface through *B*-spline or Bézier curves that allow for a large design space, while resulting in a large number of design variables. A different approach is used in this work, which benefits from the

choice of keeping the same airfoil shape during the optimization. Therefore, only the shape of the blade is modified by varying some constructive parameters of each spanwise section extracted from the original CAD model: for example, the airfoil chord, twist, sweep, and dihedral angles. By acting on these parameters, which can be selected as design variables, it is possible to perturb the blade surface in a continuous way.

To reduce the number of design variables, the constructive parameters are prescribed only at three sections of the blade portion to be optimized: the inboard section, the outboard section, and a user-defined intermediate section, as sketched in Fig. 2a. For a shape optimization over the whole blade, the inboard and outboard sections coincide with the root cutout and the blade tip, respectively. Then the blade chord and twist distributions and the leading-edge line are defined using interpolation spline functions involving their values at the prescribed sections. The complete parameterization module is based on 16 parameters: that is, four for each of the three considered sections, the spanwise location of the intermediate section, a parameter for setting the type of interpolating function, the blade radius, and the propeller angular velocity. As far as the surface and volume grid generation is concerned, a preprocessor module updates the constructive parameters at the prescribed spanwise sections starting from the design variables. Then the surface and volume CFD mesh are regenerated by using transfinite interpolation with suitable exponential blending functions. In [1], in which the outer part of the propeller blade was optimized, 14 design variables were used in the exploration of the design space, and only six design variables, the most effective ones, were selected for the multi-objective optimization. In the present work, the region of the blade under the exhaust influence is optimized requiring only two parameters: the chord and the twist at the intermediate section. The azimuthal position of the exhaust is used as an additional design variable during the optimization process, as shown in Fig. 2b.

D. Constraints

A set of geometrical and performance constraints are considered. The geometrical constraints come from the design space related to the variations of quantities such as built-in twist, sectional chord, and leading-edge line definition. In this phase of the design, quite large variations are considered and more stringent constraints, such as those imposed from mold modifications, are left to a subsequent phase. The performance constraints are relative to the shaft power availability, which is set to 633.8 kW for the takeoff condition and to 596.6 kW for the cruise condition.

E. Multi-Objective Optimization Strategy

The problem under consideration is the optimization of the propeller configuration based on the modification of the blade shape and exhaust position, so that the radiated noise is reduced at takeoff condition and the aerodynamic performances at cruise condition are not downgraded. The order in which the objectives are presented also

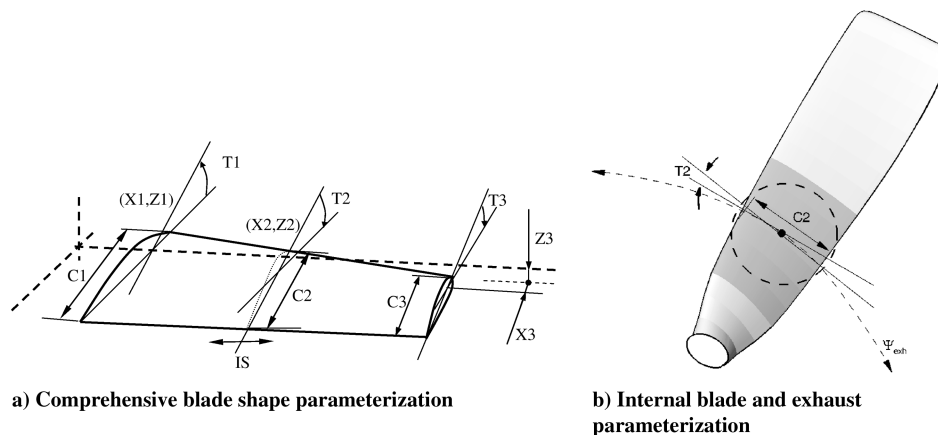


Fig. 2 Design variables for the blade propeller optimization problem.

reflects a priority in the sense that it is desirable to address both these objectives; however, although the primary necessity is to reduce the noise impact, small gains in efficiency or even small performance degradations could be accepted. The opposite situation (that is, an increase in aerodynamic efficiency resulting in a noisier configuration) is not allowed.

The noise-reduction criterion used in the aeroacoustic optimization process is the minimization of the acoustic energy on a 20-m-diam semisphere surrounding the propeller.

The proper way to address this multi-objective optimization problem consists of finding a vector of design variables so that a vector of objective functions is minimized, while a set of geometric/performance constraints bounds the problem. The process converges toward a family of optimal solutions, clustered around the so-called Pareto front in the space of the design variables. The choice of the design optimal solution then relies on a tradeoff between the conflicting objectives.

In [1] it was emphasized that the exhaust had a limited aerodynamic influence on the outer part of the blade. In practice, the sudden and strong variation of the blade loads in the exhaust region was not observed in the outer part of the blade ($r/R > 0.75$). This has suggested decoupling the optimization of the inboard part of the blade from the outer part, with the major advantage of retaining the outcome of the optimization work already performed. Thus, the optimization strategy pursued in this work is based on the following steps:

- 1) A DOE investigation of the blade inner part is carried out with a twofold aim: the outline of the most promising regions of the design space and the preparation of a database for the construction of the response surface.
- 2) An optimization based on evolutionary algorithms and exploiting the RSM is applied to select an optimal design.
- 3) The full MDA process is used to analyze the optimal design and thus verify that the RSM-predicted gains are confirmed.
- 4) The azimuthal position of the exhausts is modified and the corresponding noise levels are computed.
- 5) If the inboard blade shape and the exhaust azimuthal position separately provide a noise reduction, a further optimization is carried out starting from a hybrid blade incorporating the shape modifications obtained in [1] and step 2 and using the full MDA process.

IV. Aerodynamic Model

The CFD code used in the present study is HELIFPX [18], developed in the framework of the EC-funded project ROSAA (Rotorcraft Simulations with Advanced Aerodynamics) [19] and further improved by CIRA. It is an unsteady aerodynamic potential flow solver based on a zonal approach in which an inviscid full-potential model, a boundary-layer module, a viscous–inviscid interaction method, and a grid generator are integrated to model the flow about complex multibladed rotors.

The most relevant features of HELIFPX are as follows:

- 1) The governing equations are cast in conservative form in the inertial frame of reference.
- 2) A streamwise density flux biasing is applied to avoid nonphysical solutions (expansion shocks) and to stabilize the computation in supersonic flow regions.
- 3) Entropy and vorticity corrections are implemented taking into account, respectively, shock-generated entropy and vorticity.
- 4) The equation is discretized so that the resulting numerical scheme is first order in time and second order in space for subsonic regions and first order in space for supersonic regions.
- 5) The discretized equation is solved using an approximate factorization (AF3) technique with upwinding in supersonic regions.

The code takes advantage of the strong viscous–inviscid coupling with a boundary-layer internal module which is based on the thin-layer approximation of the Navier–Stokes equations by means of the Le Bailleur's defect-formulation theory [5,6,20,21]. This original formulation splits the system of Reynolds-averaged Navier–Stokes (RANS) equations at all points in two exactly equivalent systems: the

viscous defect-formulation system and the pseudo-inviscid-flow system, both being solved in the same physical domain. The numerical viscous–inviscid strong coupling algorithm consists of correcting the inviscid field using a wall mass flux calculated by the viscous solver and implemented through a transpiration velocity technique. Iterations between the viscous solution and the full-potential field are performed at each time step and at each coupling node, both on the wall and the wake branch. Moreover, the code makes use of a Clebsch variable model [22] to take into account the generation of vorticity caused by strong shock waves that violate the irrotational assumption of the potential formulation. For the sake of the present work, which is focused on the MDA process rather than the specifics of each involved discipline, only the underlying elements of the full-potential flow model and numerical discretization are provided, followed by validation tests carried out for a transonic propeller configuration and a helicopter rotor.

Consider a compressible inviscid perfect isentropic irrotational gas mean flow, so that $a^2 = \gamma p / \rho = \gamma \mathcal{R} T$, where γ and \mathcal{R} are the ratio of heats and the gas constant, respectively, and a , p , ρ and T are the flow sound speed, pressure, density, and temperature, respectively. The hypothesis of irrotational flow allows introducing the velocity potential ϕ , so that $\mathbf{v} = \nabla \phi$. The flow dynamics is therefore described by the continuity equation $\rho_t + \nabla \cdot (\rho \mathbf{v}) = 0$ and by the generalized Bernoulli's equation $a^2 = 1 - (\gamma - 1)(\phi_t + v^2/2)$, with the subscript t denoting the partial time derivative. By introducing a generalized coordinate system $(\xi, \eta, \zeta, \text{ and } \tau)$ fixed with the body, the governing equations can be written as

$$(\rho/J)_t + \nabla \cdot (\rho \mathbf{Q}/J) = 0 \quad (1)$$

$$a^2 = 1 - (\gamma - 1)[\phi_t + (\mathbf{Q} + \boldsymbol{\sigma}_t) \cdot \nabla \phi/2] \quad (2)$$

where $\mathbf{Q} = \boldsymbol{\sigma}_t + HH^T \nabla \phi$ is the contravariant velocity vector, H is the Jacobian matrix of the coordinate transformation, J is the determinant of H , and $\boldsymbol{\sigma}_t = H \mathbf{x}_t$ is the apparent velocity vector. Equation (1) is discretized in time by means of an implicit scheme leading to the linear system $L(\phi^{n+1} - \phi^n) = R$, where

$$L = \left\{ I + \Delta \tau \mathbf{Q} \cdot \nabla - \frac{\Delta \tau^2 a^2 J}{\rho} \left[\frac{\partial}{\partial \xi} \left(\frac{\rho g_{11}}{J} \right) \frac{\partial}{\partial \xi} + \frac{\partial}{\partial \eta} \left(\frac{\rho g_{22}}{J} \right) \frac{\partial}{\partial \eta} + \frac{\partial}{\partial \zeta} \left(\frac{\rho g_{33}}{J} \right) \frac{\partial}{\partial \zeta} \right] \right\} \quad (3)$$

$$R = \Delta \tau^2 \left(\frac{a^2 J}{\rho} \right)^n \left[\frac{(\phi^n - \phi^{n-1})}{\Delta \tau} + \nabla \cdot \left(\frac{\rho^* \mathbf{Q}}{J} \right)^n + (\phi^n - \phi^{n-1}) + \Delta \tau \left(\frac{\rho}{a^2 J} \right)^{n-1} \left(\frac{a^2 J}{\rho} \right)^n \times \left[\frac{\phi^n - 2\phi^{n-1} - \phi^{n-2}}{\Delta \tau} + \mathbf{Q}^{n-1} \cdot \nabla (\phi^n - \phi^{n-1}) \right] \right] \quad (4)$$

where g_{11} , g_{22} , and g_{33} denote the diagonal elements of the metric tensor HH^T , and ρ^* denotes the so-called retarded density, which is introduced to ensure that shock waves are better captured. As suggested in [23,24], the time derivative $(\rho/J)_t$ for deforming grid applications can be computed by exploiting the formula

$$(\rho/J)_t = \rho_t/J - \rho[(\xi_t/J)_\xi + (\eta_t/J)_\eta + (\zeta_t/J)_\zeta]$$

HELIFPX has been fully validated against experimental data, mainly coming from wind-tunnel campaigns on rotary wings carried out during several European projects. Among others, two validation cases are described hereafter. The first one is the so-called low-speed propeller of the SNAAP (Study of Noise and Aerodynamics of Advanced Propellers) project [25]. It is a six-blade transonic propeller of radius $R = 0.4495$ m advancing at a Mach number of 0.7 and rotating at an angular velocity of 410.7 rad/s. Figure 3 shows the effect of the Clebsch correction on the chordwise shock location

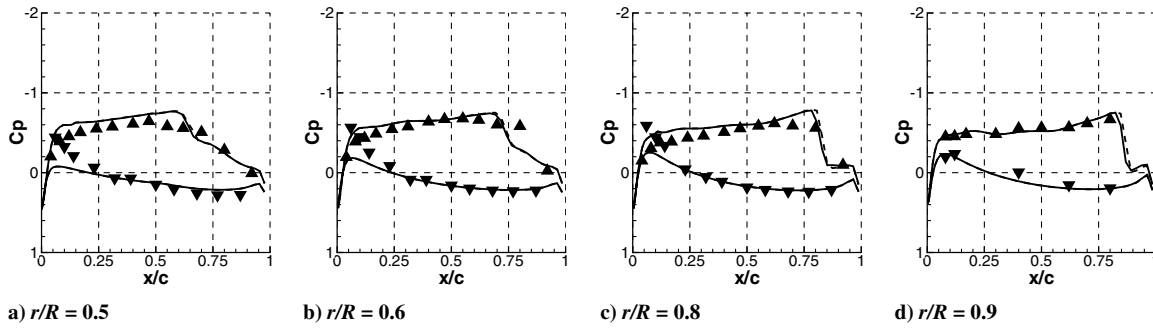


Fig. 3 Pressure coefficient at different radial stations for the SNAAP propeller (advance Mach number $M_0 = 0.7$, number of blades $B = 6$, blade radius $R = 0.4495$ m, angular velocity $\Omega = 410.7$ rad/s). Experimental data (symbols), full-potential plus entropy correction (dashed line), and full-potential plus entropy and vorticity (Clebsch) corrections (solid line). Wherever not distinguishable, lines are superimposed.

at different radial stations. A fairly good agreement with the experimental data is obtained in terms of pressure coefficient. The second validation case is the EC/ONERA 7A rotor experimentally investigated in the HELISHAPE project [26]. The rotor of radius $R = 2.1$ m operates at a medium speed forward and level flight with advance ratio $\mu = 0.355$, thrust coefficient $C_T = 0.0071$, and rotational velocity $M_{\Omega R} = 0.616$. Figure 4 shows the pressure coefficient at the radial station $r/R = 0.92$ for different azimuthal locations. The numerical results obtained with increasing physical sophistication level exhibit a consistent behavior, the better results being obtained by using a viscous-flow model and an elastic blade. The same trend is confirmed by the normal force coefficient at different radial stations plotted in Fig. 5.

V. Structural-Dynamic Model

The propeller structural-dynamic model is provided by the multibody CSD code HELTRIM. Its formulation allows accounting for mutual interaction effects due to blade aerodynamics, rigid

motion, and twist deformation. The local unsteady aerodynamic forces and moments are predicted using indicial formulation [27], and the induced velocity field is evaluated using the Mangler–Squire inflow model [28], which makes use of the incompressible linearized Euler equation to relate the pressure field across the disk plane to the induced velocity distribution. A finite element discretization of the torsional variational problem is used to compute the blade deformation induced by simple twisting. The embedded aerodynamic model can be replaced by a coupling with a CFD code, as carried out in the present work.

Since the purely CSD formulation can be verified through elementary numerical tests, it is more interesting to report the results of a validation test of the coupled CSD–CFD model. Experimental data from wind-tunnel measurements undertaken in the framework of the EC-funded project HeliNOVI [29] are used. The test case is a BO105 helicopter wind-tunnel model having a radius scale factor of 2.456 and a rotor angular speed of 110 rad/s. As shown in Fig. 6a, the use of a more accurate aerodynamic model provided by the coupling with the CFD code results in a significant improvement of

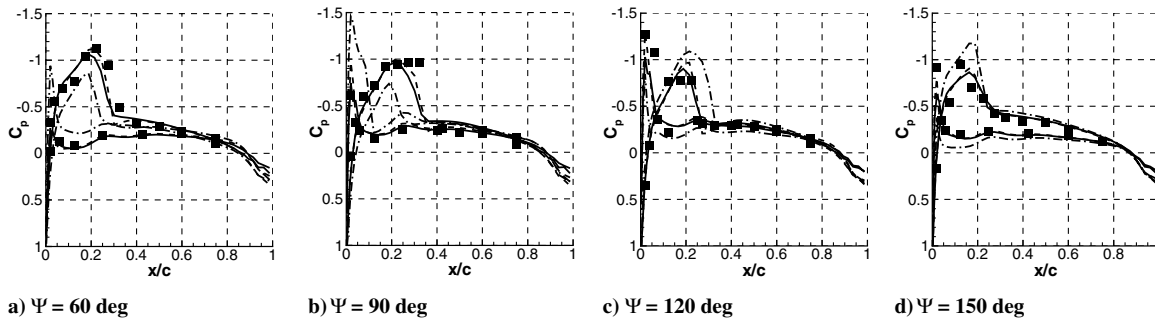


Fig. 4 Pressure coefficient at the radial station $r/R = 0.92$ and different azimuthal locations for the EC/ONERA 7A rotor (advance ratio $\mu = 0.355$, number of blades $B = 4$, blade radius $R = 2.1$ m, angular velocity $\Omega = 101.997$ rad/s). Experimental data (symbols), inviscid-flow/rigid-blade results (dashed-dotted line), inviscid-flow/elastic-blade results (dashed line), viscous-flow/elastic-blade results (solid line). Wherever not distinguishable, lines are superimposed.

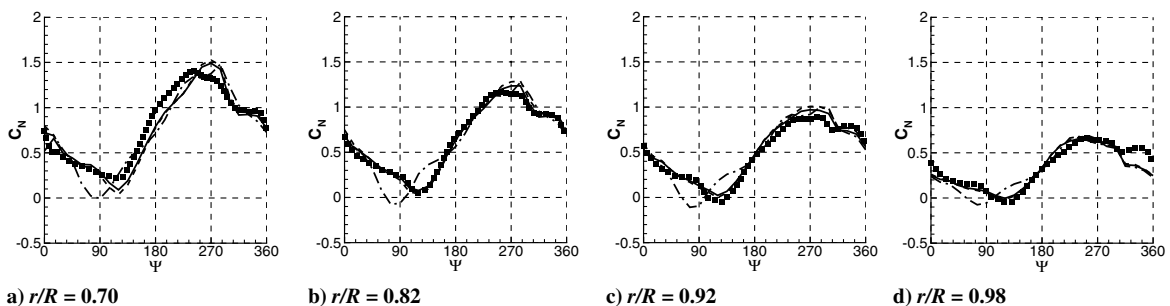


Fig. 5 Normal force coefficient at different radial stations for the EC/ONERA 7A rotor (advance ratio $\mu = 0.355$, number of blades $B = 4$, blade radius $R = 2.1$ m, angular velocity $\Omega = 101.997$ rad/s). Experimental data (symbols), inviscid-flow/rigid-blade results (dashed-dotted line), inviscid-flow/elastic-blade results (dashed line), viscous-flow/elastic-blade results (solid line). Wherever not distinguishable, lines are superimposed.

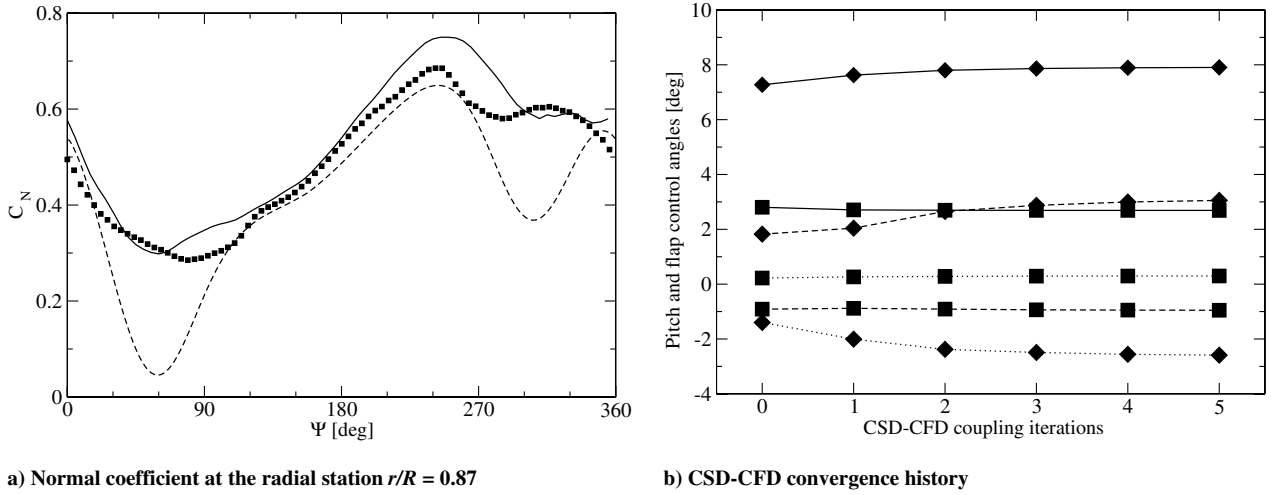


Fig. 6 HeliNOVI BO105 low-speed climb test case (advance ratio $\mu = 0.15$, climb angle $\tau = 12^\circ$, number of blades $B = 4$, blade radius $R = 2$ m, angular velocity $\Omega = 110$ rad/s). On the left, comparison between experimental data (symbols), CSD prediction (dashed line), and CSD-CFD coupled prediction (solid line). On the right, convergence behavior of the pitch angle (diamond symbols) and flap angle (square symbols) in terms of their mean values (solid line), first harmonic cosine term (dashed line) and first harmonic sine term (dotted line).

the numerical prediction. The CSD-CFD coupling usually converges within four–five iterations, as illustrated in Fig. 6b, in which the behaviors of the pitch and flapping angles, both expressed in terms of their mean and first harmonic values, are plotted.

VI. Aeroacoustic Model

The aeroacoustic model used in the present study consists of two distinct tools: the first one provides the noise signals from the computed unsteady CFD solution and body kinematics and the second one computes the noise spectra due to turbulence in proximity of the leading edge (ingested turbulence) and trailing edge (boundary-layer turbulence). Since the CFD solution accounts for the periodic flow unsteadiness due to the nonaxial flight and jet-propeller interaction, the first tool is used to compute the tonal part of the radiated noise. In contrast, the second tool exploits a statistical representation of the turbulent fluctuations about the propeller blades and is therefore suited for estimating the broadband noise levels.

A. Tonal Noise

The tonal noise generated by the propeller is computed by means of the FW-H solver OLA [30] (Object-Oriented Library for Aeroacoustics). OLA has been recently developed at CIRA by rewriting (in the C++ language) all the older tools based on Kirchhoff and FW-H formulations [31,32] and by adding two new functionalities: the porous formulation [33,34] and the marching-cube algorithm for supersonic rotating domains [35].

For the sake of the present study, the retarded-time formulation 1A [8] is employed, and the linear terms (the so-called thickness and loading noise contributions) are computed through integrals on the blade surface. The quadrupole contribution due to the nonlinear terms distributed in the perturbed field around the blade is neglected. The linear terms read as follows:

Thickness noise:

$$4\pi p'_T(\mathbf{x}, t) = \iint_S \left[\frac{\rho_0 (\dot{V}_n + V_n)}{r(1 - M_r)^2} \right]_{\text{ret}} dS_y + \iint_S \left[\frac{\rho_0 V_n (r\dot{M}_r + a_0(M_r - M^2))}{r^2(1 - M_r)^3} \right]_{\text{ret}} dS_y \quad (5)$$

where $r = |\mathbf{x} - \mathbf{y}(\tau)|$ is the source-to-observer distance, and \mathbf{M} of magnitude M is the Mach number vector of a source point on the blade surface S , which moves with an outward normal velocity V_n . The dotted quantities denote time derivatives with respect to the source (retarded) time $\tau = t - |\mathbf{x} - \mathbf{y}(\tau)|/a_0$. M_r is the projection of \mathbf{M} in the observer direction. Quantities in the square brackets are

evaluated at the retarded time. The subscripts a , n , and r denote, respectively, quiescent fluid quantities, quantities projected along the surface normal direction $\hat{\mathbf{n}}$, and quantities projected along the source-to-observer direction.

Loading noise:

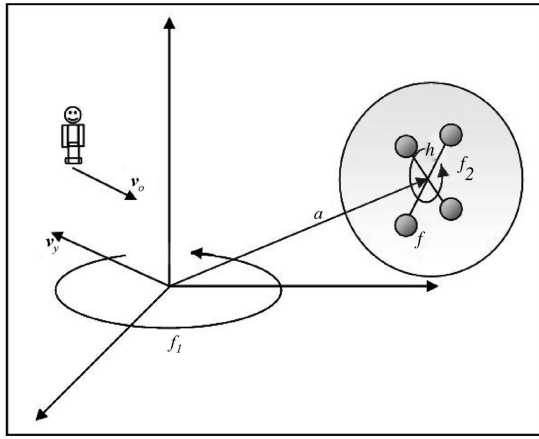
$$4\pi p'_L(\mathbf{x}, t) = \frac{1}{a_0} \iint_S \left[\frac{\dot{F}_r}{r(1 - M_r)^2} \right]_{\text{ret}} dS_y + \iint_S \left[\frac{F_r - F_M}{r^2(1 - M_r)^2} \right]_{\text{ret}} dS_y + \frac{1}{a_0} \iint_S \left[\frac{F_r(r\dot{M}_r + a_0(M_r - M^2))}{r^2(1 - M_r)^3} \right]_{\text{ret}} dS_y \quad (6)$$

where $\mathbf{F} = (p - p_0)\hat{\mathbf{n}}$ is the pressure force acting on the surface S , and F_M is the pressure force projected along the direction of the surface motion.

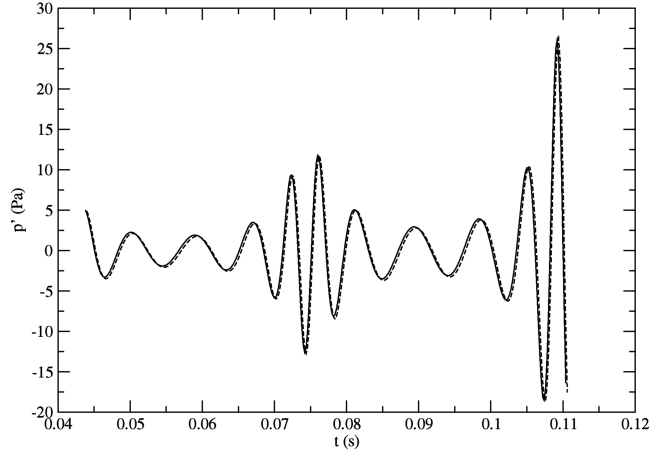
The thickness and loading noise terms provided by OLA have been verified for the more generic case of an integration upon a porous surface. The verification approach is the same as that outlined in [36]. It permits verifying the acoustic extrapolation of a perturbed near field against exact analytical solutions. Both the integrand fluctuating quantities and the far-field acoustic signals perceived by an arbitrarily moving observer are computed analytically by using elementary sources in arbitrary motion inside a moving integration surface. The test case is pictured in Fig. 7a and the corresponding noise signals are plotted in Fig. 7b. The same space–time discretization as for test case *J* of [36] has been used. The relative L_2 error with respect to the analytical solution is 5.3×10^{-3} , which is slightly higher than the reference value of 4.2×10^{-3} . The difference is probably due to the different numerical integration: a first-order integration is used in OLA, whereas a second-order Gaussian quadrature was used in the reference code.

B. Broadband Noise

The code used for the propeller broadband noise prediction is TELE-Noise, recently developed at CIRA for both rotorcraft and airframe noise applications. The code is based on semi-analytical models of the noise generated by the hydrodynamic pressure fluctuations induced by the boundary-layer turbulence in the neighborhood of a trailing edge and by the interaction between freestream turbulence convected past a leading edge. In both cases, the turbulent fluctuations can be obtained by solving the full resolved or filtered Navier–Stokes equations and then propagated to the far field through the FW-H integral approach outlined in Sec. VI.A. This approach, however, can be used only for research purposes. A viable



a) Test case layout



b) Comparison between analytical (dashed line) and numerical noise signals (solid line)

Fig. 7 Verification test of the code OLA [36]. Monopole magnitude $Q = 0.1$ kg/s, monopole frequency $f = 110$ Hz, rotational frequency around the square axis $f_2 = 43$ Hz, rotational frequency around the perpendicular axis $f_1 = 20$ Hz, system translation velocity $\mathbf{v}_y = (50, 40, 30)$ m/s, observer translation velocity $\mathbf{v}_o = (-10, -30, -50)$ m/s, radii values $a = 1$ m and $h = 0.1$ m, and observer initial position $\mathbf{x} = (10, 10, 10)$ m. The spherical integration surface is rotating at frequency f_1 .

alternative consists of using analytical models that relate near-field statistical quantities provided by a RANS solution to the statistics of the acoustic far field. Although derived from exact solutions of flat-plate acoustic scattering problems, these models can be applied to realistic geometries like wings and rotating blades. The formulation herein reported follows from the original works of [9–15].

1. Trailing-Edge Noise

Consider a blade section of chord c and span length L , as sketched in Fig. 8a. The mean flow is parallel to the x direction. The noise power spectral density reads

$$S_{pp}^{\text{TE}}(x, y, z, \omega) = \left(\frac{\bar{k}z}{2\pi\sigma^2} \right)^2 2c \int_{-\infty}^{\infty} \Phi_{pp} \left(\frac{\omega}{U_c}, k_y \right) \times \frac{\sin^2 \left[\frac{L}{c} (\bar{k}_y - \bar{k}_y/\sigma) \right]}{(\bar{k}_y - \bar{k}_y/\sigma)^2} \left| I^{\text{TE}} \left(\frac{\bar{k}}{U_c}, \bar{k}_y \right) \right|^2 d\bar{k}_y \quad (7)$$

where $\bar{k} = \omega c / (2a_0)$ is the nondimensional acoustic wave number, $\sigma = \sqrt{x^2 + \beta^2(y^2 + z^2)}$ is the Prandtl–Glauert transformed distance from the trailing edge ($\beta = \sqrt{1 - M^2}$), Φ_{pp} is the wall-pressure wave-number frequency spectrum, U_c is the boundary-layer eddy convection velocity, $\bar{k}_y = k_y c / 2$ is the nondimensional wave number in the spanwise direction, and I^{TE} is the radiation integral function. This consists of a main contribution I_1^{TE} derived from the assumption of a semi-infinite flat plate (high-frequency approximation) and a term I_2^{TE} accounting for the wave back reflection at the leading edge (finite chord length correction). These read

$$I_1^{\text{TE}} = \frac{ie^{2iC}}{C} \left\{ (1+i)e^{-2iC} \sqrt{\frac{B}{B-C}} E^*(2B-2C) - (1+i)E^*(2B) + 1 \right\} \quad (8)$$

$$I_2^{\text{TE}} = H \{ e^{4i\bar{k}} [1 - (1+i)E^*(4\bar{k})] \}^\varepsilon + H [-e^{2i\Theta^-} + i(\Theta^- + \bar{k}_x + M\bar{\mu} - \bar{k})G] \quad (9)$$

where $\bar{k}_x = k_x c / 2$ is the nondimensional wave number in the streamwise direction, $M = U_0 / a_0$ is the mean-flow Mach number, $\bar{\mu} = \omega c / (2a_0\beta^2)$,

$$E^*(\xi) = \int_0^\xi \frac{e^{-it}}{\sqrt{2\pi t}} dt$$

is the Fresnel integral, and the notation $\{\}^\varepsilon$ means that the imaginary part must be multiplied by a factor $\varepsilon = 1/\sqrt{1 + 1/(4\bar{k})}$. The other functions are defined as follows:

$$\begin{aligned} B &= \bar{K}_x - M\bar{\mu} + \bar{k}, & C &= \bar{K}_x - \bar{\mu}(x/\sigma - M), \\ H &= \frac{(1+i)e^{-4i\bar{k}}(1-\Theta^2)}{2\sqrt{\pi}(\alpha-1)\bar{k}_x\sqrt{B}}, & \Theta^- &= \bar{k} - \bar{\mu}x/\sigma \\ G &= (1+\varepsilon)e^{i(2\bar{k}+\Theta^-)} \frac{\sin(\Theta^- - 2\bar{k})}{\Theta^- - 2\bar{k}} \\ &+ (1-\varepsilon)e^{i(-2\bar{k}+\Theta^-)} \frac{\sin(\Theta^- + 2\bar{k})}{\Theta^- + 2\bar{k}} \\ &+ \frac{(1+\varepsilon)(1-i)}{2(\Theta^- - 2\bar{k})} e^{4i\bar{k}} E^*(4\bar{k}) - \frac{(1-\varepsilon)(1+i)}{2(\Theta^- + 2\bar{k})} e^{-4i\bar{k}} E^*(4\bar{k}) \\ &+ \frac{e^{2i\Theta^-}}{2} \sqrt{\frac{2\bar{k}}{\Theta^-}} E^*(2\Theta^-) \left[\frac{(1-\varepsilon)(1+i)}{\Theta^- + 2\bar{k}} - \frac{(1+\varepsilon)(1-i)}{\Theta^- - 2\bar{k}} \right] \end{aligned} \quad (10)$$

where $\bar{k}^2 = \bar{\mu}^2 - \bar{k}_y^2/\beta^2$, $\bar{K}_x = \omega c / (2U_c)$, and $\alpha = U_0 / U_c$ is the ratio between the boundary-layer asymptotic velocity and the eddy convection velocity. The wall-pressure wave-number frequency spectrum $\Phi_{pp}(\omega/U_c, k_y)$ in Eq. (7) can be related to the wall-pressure power spectral density $\phi_{pp}(\omega)$ and to the coherence $\gamma(\eta_y, \omega)$ between two points separated by the spanwise distance η_2 through the relationship

$$\Phi_{pp}(\omega/U_c, k_y) = \phi_{pp}(\omega) l_y(\omega, k_y) / \pi$$

with

$$l_y(\omega, k_y) = \int_0^\infty \gamma(\eta_y, \omega) \cos(k_y \eta_2) d\eta_2$$

The spanwise correlation length is assumed to be given by the Corcos formula $l_y(\omega, k_y) = bU_c/\omega$, with b being a calibration constant. The power spectral density $\phi_{pp}(\omega)$ can be estimated through a semi-empirical model proposed by Rozenberg [37] that takes into account the chordwise pressure gradient: that is,

$$\phi_{pp}\left(\frac{\omega\delta^*}{U_0}\right) = \frac{(\tau_w^2\delta^*/U_0)0.78(1.8\Pi\beta_c + 6)(\omega\delta^*/U_0)^2}{[(\omega\delta^*/U_0)^{0.75} + 0.105]^{3.7} + [3.76Re_T^{-0.57}(\omega\delta^*/U_0)]^7} \quad (11)$$

where δ^* denotes the boundary-layer displacement thickness, τ_w is the wall shear stress, $Re_T = u_\tau\delta\sqrt{C_f/2}/\nu$ is the weighted Reynolds number (u_τ being the friction velocity), $\beta_c = (\theta/\tau_w) dp/dx$ is the Clauser pressure gradient parameter (θ being the boundary-layer momentum thickness), and Π is the wake law parameter resulting from

$$2\Pi - \ln(1 + \Pi) = \kappa U_0/u_\tau - \ln(\delta^*U_0/\nu) - 0.51\kappa - \ln \kappa$$

where $\kappa = 0.41$ is the von Kármán constant.

2. Leading-Edge Noise

Consider the airfoil configuration sketched in Fig. 8a, with the reference system centered at the leading edge. The far-field noise spectral density due to impinging turbulent fluctuations can be written as

$$S_{pp}^{LE}(x, y, z, \omega) = \left(\frac{\rho_0 \bar{k} z}{\sigma^2}\right)^2 \pi U_0 \frac{L}{2} \int_{-\infty}^{\infty} \Phi_{ww}\left(\frac{\omega}{U_0}, k_y\right) \times \frac{\sin^2\left[\frac{L}{2}\left(\frac{k_y}{\sigma} - k_y\right)\right]}{\frac{\pi L}{2}\left(\frac{k_y}{\sigma} - k_y\right)^2} \left|I_1^{LE}\left(x, \frac{\omega}{U_0}, k_y\right)\right|^2 dk_y \quad (12)$$

where the radiation integral I_1^{LE} takes into account both the main leading-edge contribution I_1^{LE} and the trailing-edge backscattering contribution I_2^{LE} that are given by

$$I_1^{LE} = -\frac{1}{\pi} \sqrt{\frac{2}{(\bar{k}_x + \beta^2 \bar{k})\Theta^-}} e^{-i\bar{\Theta}} E(2\Theta^-) \quad (13)$$

$$I_2^{LE} = \frac{e^{-i\bar{\Theta}}}{\pi \Theta^- \sqrt{2\pi(\bar{k}_x + \beta^2 \bar{k})}} \times \left\{ i(1 - e^{2i\Theta^-}) - (1 + i) \left[E(4\bar{k}) - e^{2i\Theta^-} \sqrt{\frac{2\bar{k}}{\Theta^+}} E(2\Theta^+) \right] \right\} \quad (14)$$

where $\Theta^\pm = \bar{k} \pm \bar{\mu}x/\sigma$, and $\bar{\Theta} = \bar{k}_x(1 - Mx/\sigma)/\beta^2 - \pi/4$. The velocity wave-number frequency spectrum of the impinging upward velocity $\Phi_{ww}(\omega/U_0, k_y)$ can be related to the velocity power spectral density $\phi_{ww}(\omega)$ and spanwise correlation length $l_y(\omega, k_y)$ through the relationship

$$\Phi_{ww}(\omega/U_0, k_y) = U_0 \phi_{ww}(\omega) l_y(\omega, k_y) / \pi$$

Then the impinging turbulent fluctuations can be modeled as frozenly convected homogeneous isotropic turbulence ($\omega = k_x U_0$) described by a von Kármán spectrum: that is,

$$\phi_{ww}(k_x) = \frac{\bar{u}^2 L_t}{2\pi U_0} \frac{1 + \frac{8}{3}(k_x/k_e)^2}{[1 + (k_x/k_e)^2]^{21/6}} \quad (15)$$

$$l_y(k_x) = \frac{8L_t}{3} \left[\frac{\Gamma(1/3)}{\Gamma(5/6)} \right]^2 \frac{(k_x/k_e)^2}{[3 + 8(k_x/k_e)^2] \sqrt{1 + (k_x/k_e)^2}}$$

where $k_e = (\sqrt{\pi}/L_t)\Gamma(5/6)/\Gamma(1/3)$ is the wave number of maximum turbulent kinetic energy, Γ is the gamma function, \bar{u}^2 is the mean square value of the turbulent velocity fluctuations, and L_t is the turbulence integral scale. Both \bar{u}^2 and L_t can be related to the Reynolds-averaged turbulent kinetic energy K and dissipation rate ϵ by writing $\bar{u}^2 = 2K/3$ and $L_t = 0.4K^{1.5}/\epsilon$.

3. Broadband Noise Model Validation

The trailing-edge noise model can be validated by using the airfoil self-noise data collected by Brooks and Hodgson [38]. A NACA-0012 airfoil of chord $c = 0.6096$ m and span $L = 0.46$ m at zero incidence is considered for two freestream velocities: $U_0 = 69.5$ and 38.6 m/s. The measured boundary-layer quantities are $\delta^* = 4 \times 10^{-3}$ m and $U_c = 0.6U_0$ for both cases and $b = 1.724$ and 1.613 for the higher and lower freestream velocities, respectively. The sound pressure levels at a distance of 1.2 m from the trailing edge are shown in Fig. 9a. The higher-value curves correspond to the higher freestream velocity. The semi-analytical results have been obtained by using two different approaches: the first one consists of using the measured wall-pressure spectrum and spanwise correlation length close to the trailing edge, and the second one consists of using Rozenberg's [37] semi-empirical wall-pressure spectrum model computed on the base of the boundary-layer quantities provided by Le Balleur's [5,6] thin-layer viscous model of the CFD code HELIFPX. Therefore, the second approach provides a full validation of the aeroacoustic broadband noise model employed in the present work. It can be observed that both the frequency and velocity trends of the noise levels are quite well predicted, which is mostly relevant for an optimization process. Furthermore, the noise levels are predicted with an accuracy of about 3–4 dB. Indeed, the underestimation of the noise levels is likely to be due to the fact that Brooks and Hodgson [38] measured both the airfoil trailing-edge noise and the jet-turbulence interaction noise that should have roughly the same levels, thus justifying a factor 2 in the noise prediction.

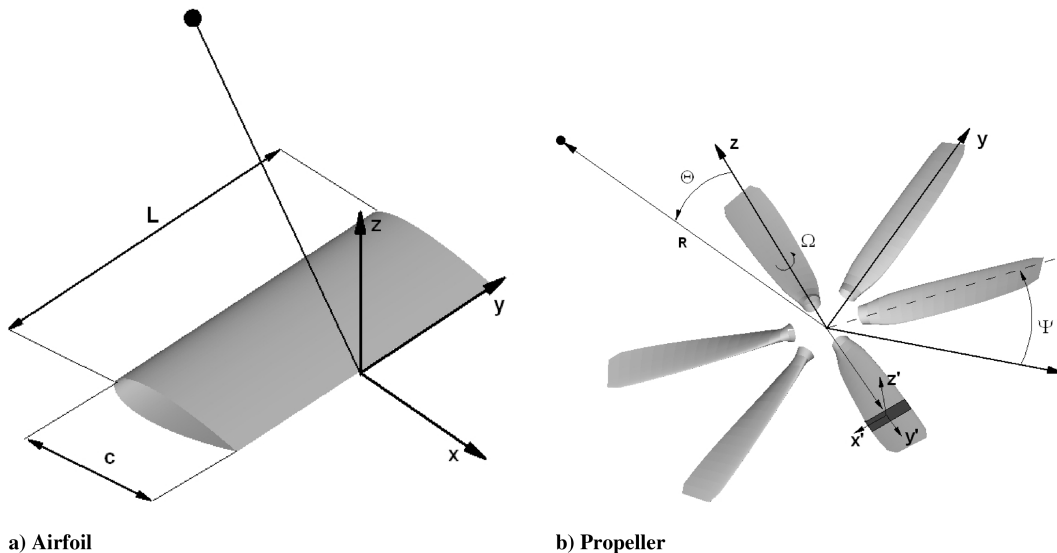


Fig. 8 Coordinate systems and notation used for the airfoil broadband noise model and extension to a propeller configuration.

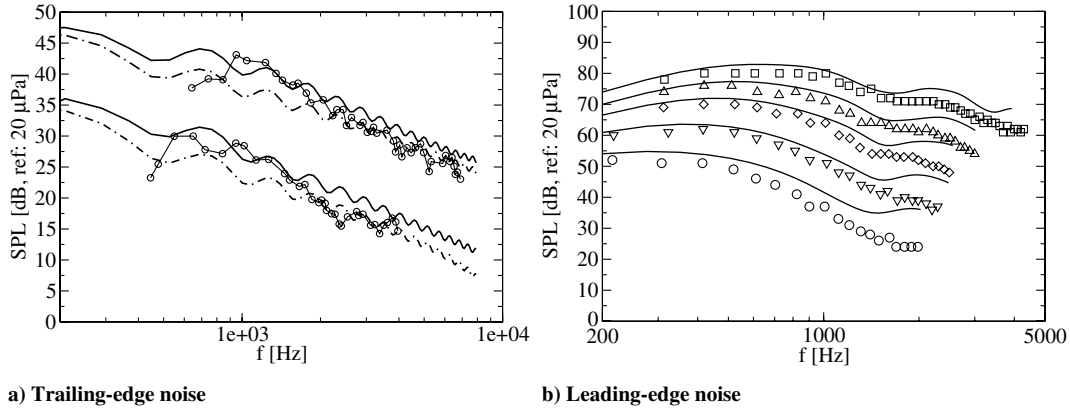


Fig. 9 Airfoil broadband noise results. On the left, NACA-0012 self-noise measurements [38] (symbols) are compared with semi-analytical results obtained by using the measured wall-pressure spectrum (solid line) and the semi-empirical computed wall-pressure spectrum (dashed-dotted line). On the right, NACA-0012 interaction-noise measurements [10] (symbols) are compared with semi-analytical results (lines) at different freestream velocities (\square : 165 m/s, \triangle : 120 m/s, \diamond : 90 m/s, ∇ : 60 m/s, and \circ : 40 m/s).

The leading-edge noise model can be validated by using the airfoil turbulence interaction-noise data collected by Paterson and Amiet [10]. A NACA-0012 airfoil of chord $c = 0.23$ m and span $L = 0.53$ m at zero incidence and five freestream velocities in the range of 40–165 m/s is considered. The sound pressure levels at a distance of 2.25 m from the leading edge are shown in Fig. 9b. The semi-analytical results have been obtained by assuming the measured turbulence intensity and integral length scale and by taking into account the shear-layer refraction effects. It is again worthwhile to observe that the frequency and velocity trends of the noise levels are quite well predicted and that the confidence level of the prediction is about 3 dB in the maximum noise frequency range.

4. Extension to a Rotating Blade

To extend the airfoil broadband noise models to a propeller blade, a strip theory is applied. The blade is segmented in a number of spanwise elements, as shown in Fig. 8b, and for each of them, the corresponding 2-D mean-flow, turbulent quantities, and radiation angles are extracted from the HELIFPX solution file. In addition, a frequency-shift correction is applied to each section to account for the Doppler effects by writing

$$\omega_e(\Psi)/\omega = 1 + M_t \sin \Theta \sin \Psi / \sqrt{1 - M_z^2 \sin^2 \Theta}$$

where M_t and M_z are the tip and axial Mach numbers, respectively, of the blade section. Finally, the overall propeller noise is computed by assuming uncorrelated strip sources and averaging over all the angular positions of the B propeller blades: that is,

$$S_{pp}(\mathbf{x}, \omega) = \frac{B}{2\pi} \int_0^{2\pi} \frac{\omega_e(\Psi)}{\omega} S_{pp}^\Psi(\mathbf{x}, \omega_e) d\Psi \quad (16)$$

VII. Optimization Results

Before addressing the optimization problem, it is interesting to assess the different tonal and broadband competing noise mechanisms for the reference pusher-propeller configuration. Figure 10 shows the sound pressure noise-directivity patterns computed at a certain distance from the propeller center on a plane containing the propeller axis that corresponds to the radiation angle 90 deg.

The broadband noise contributions plotted in Figs. 10a and 10b have been computed for the installed baseline propeller by feeding TELE-Noise with the mean-flow and boundary-layer quantities computed by HELIFPX. Furthermore, the interaction noise has been computed by estimating the exhaust turbulence level and integral scale by means of a separate RANS jet simulation; an axisymmetric jet at the same exhaust conditions has been considered and the average levels of K and ϵ have been extracted at the same nozzle/

propeller distance. Along the angular sectors for which no blade–exhaust interaction occurs, typical values of ingested atmospheric turbulence have been used. The tonal noise contributions have been computed by considering an isolated propeller (for which the only significant unsteady mechanism is due to the nonaxial flight speed) and the installed propeller (for which the dominant unsteady mechanism is due to the blade–exhaust interaction). It is interesting to observe that the overall broadband noise is about 40 dB higher than the trailing-edge noise and that the tonal noise generated by the installed propeller overwhelms both the broadband noise and the tonal noise in the absence of blade–exhaust interactions (apart from the blade passage frequency peak). Therefore, it can be reasonably asserted that the optimization process presented hereafter is mostly driven by the minimization of the tonal noise.

In [1], an optimized blade was obtained, referred to here as optim-1, providing a reduction of 1.5 dB of the acoustic energy computed on a 20-m-diam semisphere surrounding the propeller. This blade was characterized by modifications of twist, chord, and sweep angle (see Fig. 11b), mainly in its outboard part (Fig. 11a). In the same paper, the authors argued that the optimization process would have been further enhanced by including, among the design variables, the chord and the twist of the blade sections interacting with the exhaust jet. In addition, it was envisioned that the shape and the position of the exhaust could have a role in further reducing the acoustic impact of the propeller.

The hypothesis according to which the exhausts have a limited impact on the outer part of the blade suggests to decouple the optimization of the inner part of the blade from the outer part. Since the parameterization module allows the user to chose the part of the blade to be parameterized, that part is made coincident with the blade region under the exhaust influence. A DOE based on 100 elements has been scheduled, with the Latin hypercube method requiring the involvement of the full MDA process. The design variables are the twist and chord at the middle section of the considered region, denoted throughout as T2 and C2, respectively. The parameters T2 and C2 are varied in the ranges of $[-40\%:40\%]$ and $[-25\%:25\%]$, respectively, of their nominal values.

Figure 12a shows the combination of T2 and C2 for which the computations are performed, and Fig. 12b shows the corresponding results in terms of acoustic energy at the takeoff and cruise efficiency. A computationally expensive DOE is exploited to generate the surrogate models (RSM), shown in Fig. 13, to be subsequently used for the optimization.

By looking at the response surfaces of Fig. 13a, it can be observed that a reduction of the acoustic energy is achieved in the region in which T2 increases and C2 decreases. In contrast, as shown by Fig. 13b, higher values of T2 tend to downgrade the cruise efficiency, and less clear indications can be drawn for the chord influence. Once again, there exist conflicting choices and the multi-objective optimization can play a crucial role in the tradeoff analysis.

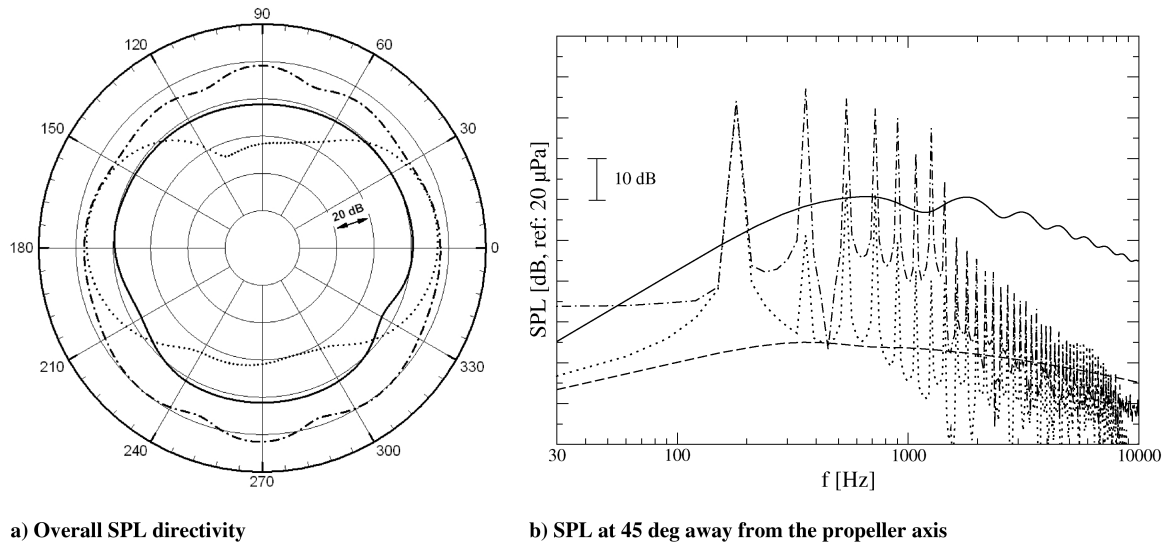


Fig. 10 Computed propeller noise-directivity patterns and sound pressure level spectra ($\Delta f = 30$ Hz). Comparison between: tonal noise (dashed-dotted line), tonal noise with no exhaust (dotted line), overall broadband noise (solid line), and trailing-edge noise (dashed line).

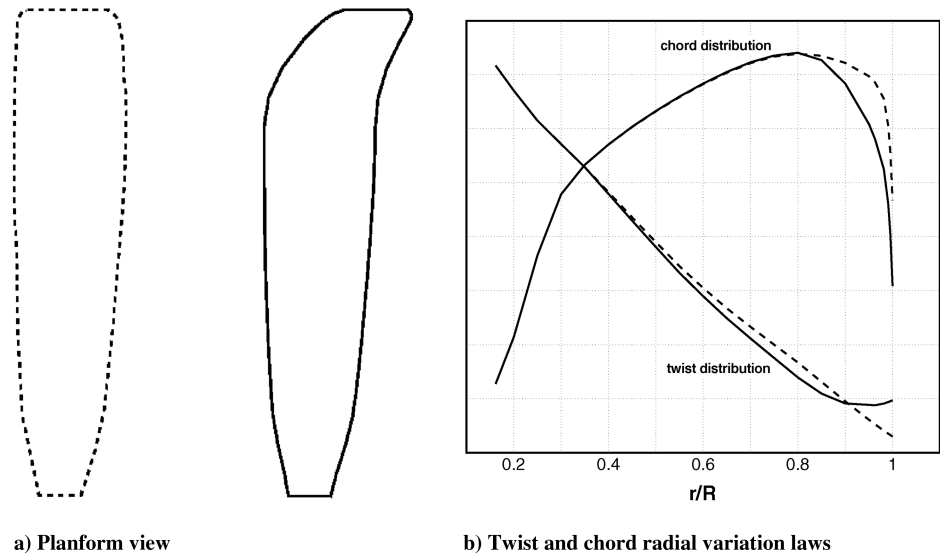


Fig. 11 Comparison between reference (dashed line) and optim-1 (solid line) blades.

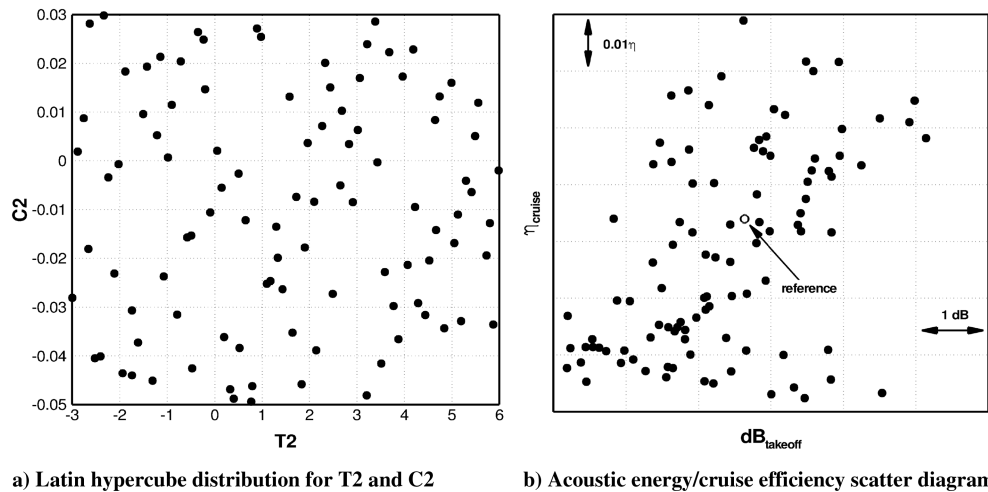


Fig. 12 Collection of DOE results for the inner part of the blade.

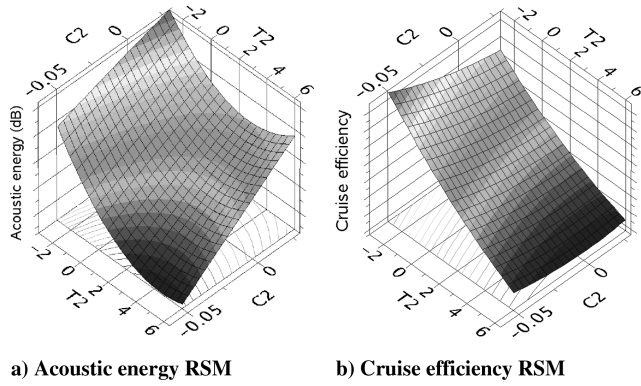


Fig. 13 Response surfaces as a function of the design variables T2 and C2.

A multi-objective optimization problem has been set up by requiring the minimization of the acoustic energy and the maximization of the cruise efficiency. The nondominated sorting evolutionary algorithm NSEA+ has been used, and the objectives were estimated using the RSM surrogate models. The problem has been addressed through the evaluation of 80 designs. The results are shown in Fig. 14, in which the designs are collected into a scatter diagram with the objectives on the axes. In this figure the designs falling on the Pareto front are emphasized with black bullets. Among these designs, the design denoted as optim-2 has been selected, since

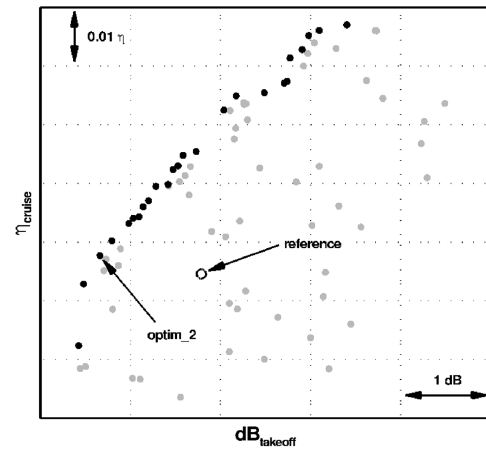


Fig. 14 Multi-objective propeller blade optimization results: overall acoustic energy on the x axis and aerodynamic cruise efficiency on the y axis.

it guarantees a reduction of about 1 dB with a small increase in the cruise efficiency.

The optim-2 blade planform and characteristics are depicted in Fig. 15. As reasonably expected, the optimization process has led to a twist increase and a chord reduction. As a matter of fact, the twist increase tends to counteract the sudden negative variation of the

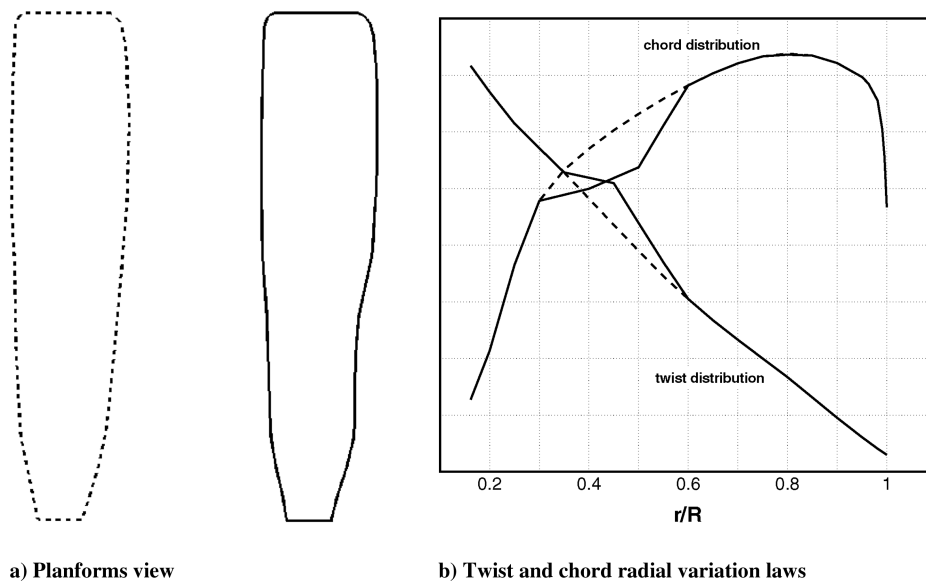


Fig. 15 Comparison between reference (dashed line) and optim-2 (solid line) blades.

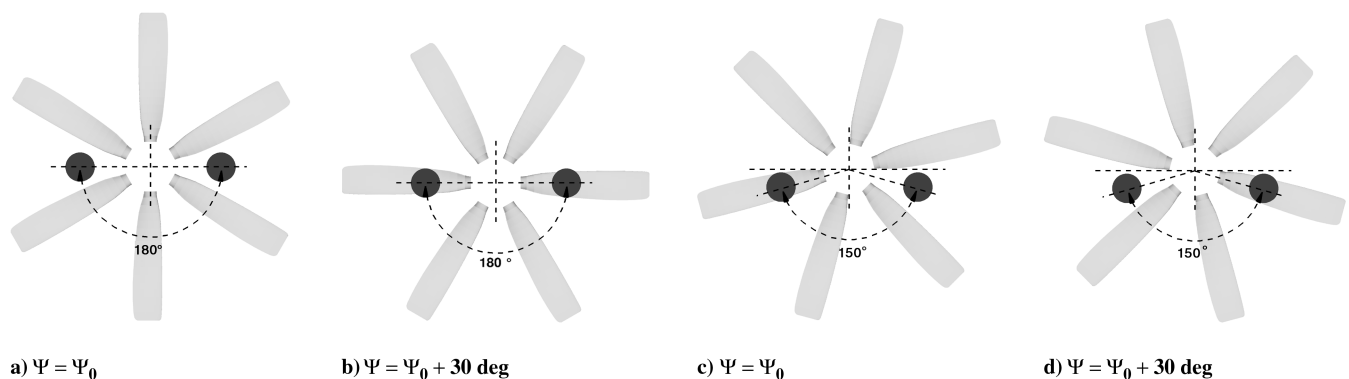


Fig. 16 Geometrical considerations about blade-exhaust interaction effects.

effective angle of attack, whereas the chord reduction tends to diminish the blade–exhaust interaction area.

As far as the exhaust shape and location are concerned, only the variation of the azimuthal relative position has been investigated, since the nozzle shape has an impact on the jet flow properties, and the radial position results from design considerations related to the blade erosion and deicing effects due to the jet impingement. Figures 16a and 16b show that for a six-blade propeller the baseline configuration characterized by two diametrically opposite exhausts results in simultaneous passage of two blades through the exhausts. In contrast, the modified configuration obtained by skewing the azimuthal location of the exhausts, even though it allows to not incur in the above problem, leads to a new distribution of the noise sources, since it may happen that there is always at least a blade under the exhaust influence. For example, Figs. 16c and 16d depict the situation when the minimum angle between the two exhausts is 150 deg. The numerical analysis of this exhaust configuration, which was chosen on the basis of a visual inspection, allows a further reduction on the radiated noise at the takeoff (−0.62 dB).

The optimization of the inboard part of the blade has been obtained under the hypothesis that the inner flow is weakly coupled with the outer one. Hence, by taking advantage from the fact that the optim-1 blade configuration shares the inboard part with the reference blade, a hybrid design referred to as optim-3 has been generated, replacing the new designed inboard part of the optim-2 blade into the optim-1 blade. The analysis of the optim-3 blade confirms that it can achieve a

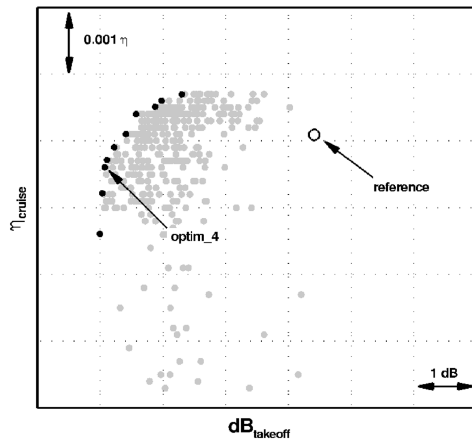


Fig. 17 Multi-objective propeller blade optimization results: overall acoustic energy on the x axis and aerodynamic cruise efficiency on the y axis.

Table 1 Comparison of aeroacoustic performances for different blade designs

Blade	Δ acoustic energy, dB	Δ cruise efficiency	$\Delta\Psi$, deg
Reference	—	—	—
Reference	−0.62	−0.009	30
optim-1	−1.50	+0.006	0
optim-2	−1.10	+0.012	0
optim-3	−2.50	−0.005	0
optim-4	−3.50	−0.0005	17.3

reduction of 2.5 dB with respect to the reference blade. However, the blade region under the exhaust influence and the azimuthal position of the exhausts in the propeller disk mutually affect each other. For this reason, by starting from the optim-3 blade, a new multi-objective problem has been set up for the same objectives; the full MDA process was used with the involvement of three design variables: T2, C2, and the exhaust azimuthal distance $\Delta\Psi$.

It has been necessary to evaluate 600 designs, requiring an overall CPU time of about 360 h on a NEC TX7 system (Itanium II processor). The designs are compared in Fig. 17 in terms of acoustic energy and cruise efficiency, and those falling on the Pareto front are, as before, emphasized with black bullets. From the optima designs on the Pareto front, the optim-4 blade has been extracted. The geometrical characteristics are illustrated in Fig. 18, and the corresponding value of the exhaust azimuthal distance is 162.63 deg.

Table 1 has been filled in with homogeneous results. All of the numerical predictions come from the application of the full MDA process (that is, the design optim-2 obtained from the RSM evaluations and the optim-3 hybrid design) have been separately recalculated by using the full MDA process.

VIII. Conclusions

The present work focused on the aeroacoustic shape optimization of a propeller blade in a pusher configuration. An existing methodology was enriched with new modules providing the propeller broadband noise levels. The whole multidisciplinary computational chain comply with the affordability required by an automatic optimization process. Although broadband noise contributions for rotors and propellers are generally nonnegligible, in the present study, the tonal noise contribution due to the high-speed flow in the tip region and the blade–exhaust interaction in the inner part of the blade plays a dominant role. The shape optimization revealed that the overall acoustic energy of the pusher propeller can be reduced up to a value of 3.5 dB. This reduction is nearly equally due to an optimal design of the blade planform in the tip and inner regions. Compared with the five-blade production propeller, the new

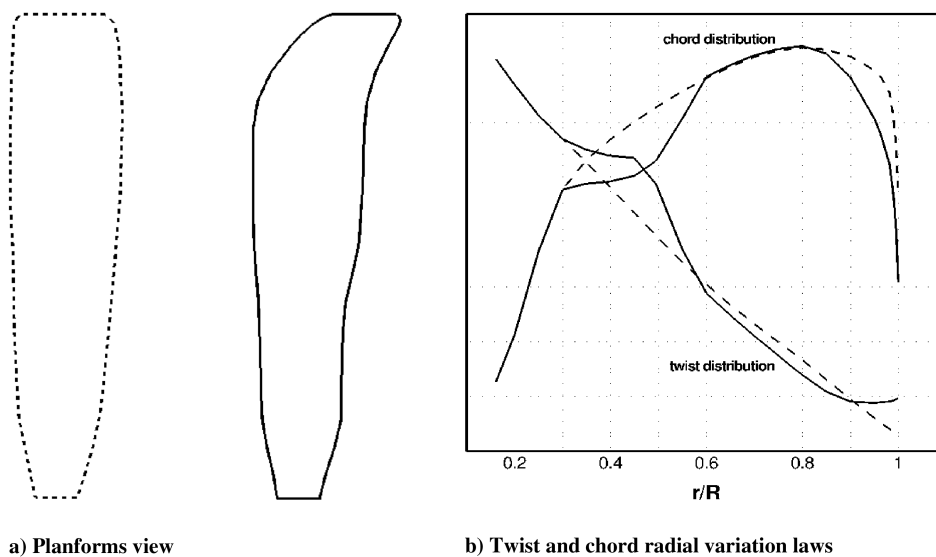


Fig. 18 Comparison between reference (dashed line) and optim-4 blades (solid line).

optimized six-blade propeller results in a 5.5 dB overall noise reduction. Finally, it is worthwhile to mention that the present analysis did not account for the noise due to the interaction between the propeller blades and the wing wake. This will be the objective of future optimization studies in which use of Navier–Stokes CFD models will be made.

Acknowledgments

This optimization activity has been carried out within the ACADEMIA project (Advanced Computational Aerodynamic Environment for Multi-Disciplinary Integrated Analysis) partially funded by the Italian Ministry for Education, University and Scientific Research. The P180 configuration has been provided by Piaggio Aero in the framework of the CESAR (Cost-Effective Small Aircraft) project funded by the European Commission.

References

- [1] Pagano, A., Federico, L., Barbarino, M., Guida, F., and Aversano, M., "Multi-Objective Aeroacoustic Optimization of an Aircraft Propeller," AIAA Paper 2008-6059, Sept. 2008.
- [2] Ianniello, S., Mascio, A. D., Salvatore, F., Sollo, A., Aversano, M., and Gennaretti, M., "Evaluation of Noise Excess for Pushing Propeller Aircraft by CFD Aeroacoustic Calculation," AIAA Paper 2004-3006, May 2004.
- [3] Marulo, F., Sollo, A., Aversano, M., Polimero, U., and Perna, F., "Measurement and Prediction of Community Noise of a Pusher-Propeller General Aviation Aircraft," AIAA Paper 2005-2984, May 2005.
- [4] Pagano, A., Leoncini, P., and Pisoni, A., "System and Software Methodologies Applied to a Rotorcraft Simulation System," *American Helicopter Society Specialists' Meeting* [CD-ROM], AHS International, Alexandria, VA, Nov. 2000.
- [5] Le Balleur, J. C., "Viscous-Inviscid Flow Matching: Numerical Method and Applications to Two-Dimensional Transonic and Supersonic Flows," *La Recherche Aérospatiale: Bulletin Bimestriel*, Vol. 1978, No. 2, 1978, pp. 65–67.
- [6] Le Balleur, J. C., "Strong Matching Method for Computing Transonic Viscous Flows Including Wakes and Separations: Lifting Airfoils," *La Recherche Aérospatiale: Bulletin Bimestriel*, Vol. 1981, No. 3, May 1981, pp. 161–185.
- [7] Ffowcs Williams, J. E., and Hawkins, D. L., "Sound Generated by Turbulence and Surfaces in Arbitrary Motion," *Philosophical Transactions of the Royal Society of London, Series A: Mathematical and Physical Sciences*, Vol. 264, No. 1151, 1969, pp. 321–342. doi:10.1098/rsta.1969.0031
- [8] Farassat, F., and Succi, G. P., "The Prediction of Helicopter Discrete Frequency Noise," *Vertica*, Vol. 7, No. 4, 1983, pp. 309–320.
- [9] Amiet, R. K., "Noise Due to Turbulent Flow Past a Trailing Edge," *Journal of Sound and Vibration*, Vol. 47, No. 3, 1976, pp. 387–393. doi:10.1016/0022-460X(76)90948-2
- [10] Paterson, R. W., and Amiet, R. K., "Acoustic Radiation and Surface Pressure Characteristics of an Airfoil Due to Incident Turbulence," NASA CR-2733, Sept. 1976.
- [11] Paterson, R. W., and Amiet, R. K., "Noise of a Model Helicopter Rotor Due to Ingestion of Turbulence," NASA CR-3213, 1979.
- [12] Schlinker, R. H., and Amiet, R. K., "Helicopter Trailing Edge Noise," NASA CR-3470, 1981.
- [13] Roger, M., and Moreau, S., "Broadband Self-Noise from Loaded Fan Blades," *AIAA Journal*, Vol. 42, No. 3, 2004, pp. 536–544. doi:10.2514/1.9108
- [14] Roger, M., and Moreau, S., "Back-Scattering Correction and Further Extensions of Amiet's Trailing Edge Noise Model, Part 1: Theory," *Journal of Sound and Vibration*, Vol. 286, No. 3, 2005, pp. 477–506. doi:10.1016/j.jsv.2004.10.054
- [15] Moreau, S., and Roger, M., "Competing Broadband Noise Mechanisms in Low-Speed Axial Fans," *AIAA Journal*, Vol. 45, No. 1, 2007, pp. 48–57. doi:10.2514/1.14583
- [16] OPTIMUS, Software Package, Ver. 5.2, Noesis Solutions, Leuven, Belgium, 2006.
- [17] Samareh, J. A., "Survey of Shape Parameterization Techniques for High-Fidelity Multidisciplinary Shape Optimization," *AIAA Journal*, Vol. 39, No. 5, May 2001, pp. 877–884. doi:10.2514/1.1458310.2514/2.1391
- [18] Hounjet, M. H. L., Le Balleur, J. C., Blaise, D., Bernardini, G., and Pisoni, A., "Maturation of a Full Potential Based Rotors Flow Field Code," *Proceedings of the 26th European Rotorcraft Forum* [CD-ROM], Netherlands Association of Aeronautical Engineers, The Hague, The Netherlands, Sept. 2000.
- [19] Miller, J. V., Pidd, M., Pagano, A., Haverdings, H., Bernardini, G., Francescoantonio, P. D., Pisoni, A., and Gracey, M., "ROSAA: The European Solution to Connect Aeroelasticity, Aerodynamics and Acoustic Codes in a Unique User-Friendly Rotorcraft Simulation System," *Proceedings of the 26th European Rotorcraft Forum* [CD-ROM], Netherlands Association of Aeronautical Engineers, The Hague, The Netherlands, Sept. 2000.
- [20] Le Balleur, J. C., and Girodroux-Lavigne, P., "A Semi-Implicit and Unsteady Numerical Method of Viscous-Inviscid Interaction for Transonic Separated Flows," *La Recherche Aérospatiale*, Vol. 1984, No. 1, Jan. 1984, pp. 15–37.
- [21] Le Balleur, J. C., and Girodroux-Lavigne, P., "Calculation of Dynamic Stall by viscous-inviscid Interaction over Airfoils and Helicopter-Blade Sections," *Proceedings of the American Helicopter Society 51st Annual Forum* [CD-ROM], AHS International, Alexandria, VA, 1995.
- [22] Westland, J., and Hounjet, M. H. L., "Clebsch Variable Model for Unsteady Inviscid Transonic Flow with Strong Shock Waves," AIAA Paper 1993-3025, 1993.
- [23] Visbal, M. R., and Gaitonde, D. V., "On the Use of High-Order Finite-Difference Schemes on Curvilinear and Deforming Meshes," *Journal of Computational Physics*, Vol. 181, No. 1, 2002, pp. 155–185. doi:10.1006/jcph.2002.7117
- [24] Daude, F., Lafon, P., Crouzet, F., and Bailly, C., "On Overset Grid Strategy for Aeroacoustics and Aeroelasticity of Moving Bodies," *International Workshop on Fluid-Structure Interaction: Theory, Numerics and Applications*, Hersching, Germany, Sept. 2008.
- [25] Schulten, J. B. H. M., "Comparison of Measured and Predicted Noise of the Brite-EuRam SNAAP Advanced Propellers," AIAA Paper 97-1709, May 1997.
- [26] Schultz, K. J., Spletstoesser, W., Junker, B., Wagner, W., Schoell, E., Arnaud, G., Mercker, E., Pengel, K., and Fertis, D., "A Parametric Wind Tunnel Test on Rotorcraft Aerodynamics and Aeroacoustics (Helishape): Test Procedures and Representative Results," *The Aeronautical Journal*, Vol. 101, No. 1004, 1997, pp. 143–154.
- [27] Leishman, J. G., and Nguyen, K. Q., "State Space Representation of Unsteady Airfoil Behaviour," *AIAA Journal*, Vol. 28, No. 5, Sept. 1990, pp. 836–844. doi:10.2514/3.25127
- [28] Leishman, J. G., *Principles of Helicopter Aerodynamics*, Cambridge Univ. Press, New York, 2006.
- [29] Langer, H.-J., Dieterich, O., Oerlemans, S., Schneider, O., Van der Wall, B., and Yin, J., "The EU HeliNoVi Project – Wind Tunnel Investigations for Noise and Vibration Reduction," *Proceedings of the 31st European Rotorcraft Forum* [CD-ROM], Associazione Italiana di Aeronautica e Astronautica, Florence, Italy, 2005.
- [30] Fitzpatrick, J. A., "Aeroacoustics Research in Europe: The CEAS-ASC Report on 2004 Highlights," *Journal of Sound and Vibration*, Vol. 288, Nos. 1–2, 2005, pp. 1–32. doi:10.1016/j.jsv.2005.05.025
- [31] Ianniello, S., "An Algorithm to Integrate the FW-H Equation on a Supersonic Rotating Domain," *AIAA Journal*, Vol. 37, No. 9, Sept. 1999, pp. 1040–1047. doi:10.2514/2.831
- [32] Ianniello, S., "Quadrupole Noise Predictions Through the Ffowcs Williams Hawkins Equation," *AIAA Journal*, Vol. 37, No. 9, Sept. 1999, pp. 1048–1054. doi:10.2514/2.832
- [33] Di Francescantonio, P., "A New Boundary Integral Formulation for the Prediction of Sound Radiation," *Journal of Sound and Vibration*, Vol. 202, No. 4, 1997, pp. 491–509. doi:10.1006/jsvi.1996.0843
- [34] Brentner, K. S., and Farassat, F., "Analytical Comparison of the Acoustic Analogy and Kirchhoff Formulation for Moving Surfaces," *AIAA Journal*, Vol. 36, No. 8, 1998, pp. 1379–1386. doi:10.2514/2.558
- [35] Brentner, K. S., "Numerical Algorithms for Acoustic Integrals with Examples for Rotor Noise Prediction," *AIAA Journal*, Vol. 35, No. 4, 1997, pp. 625–630. doi:10.2514/2.182
- [36] Casalino, D., "An Advanced Time Approach for Acoustic Analogy Predictions," *Journal of Sound and Vibration*, Vol. 261, No. 4, 2003, pp. 583–612. doi:10.1016/S0022-460X(02)00986-0

- [37] Rozenberg, Y., “Modélisation Analytique du Bruit Aérodynamique à Large Bande des Machines Tournantes: Utilisation de Calculs Moyennés de Mécanique des Fluides,” Ph.D. Thesis, Ecole Centrale de Lyon, Ecully, France, Dec. 2007.
- [38] Brooks, T. F., and Hodgson, T. H., “Trailing Edge Noise Prediction from Measured Surface Pressures,” *Journal of Sound and Vibration*, Vol. 78, No. 1, 1981, pp. 69–117.
doi:10.1016/S0022-460X(81)80158-7